

## Case History

# Hydrogeophysical investigations in the western and north-central Okavango Delta (Botswana) based on helicopter and ground-based transient electromagnetic data and electrical resistance tomography

Philip Meier<sup>1</sup>, Thomas Kalscheuer<sup>2</sup>, Joel E. Podgorski<sup>1</sup>, Lesego Kgotlhang<sup>3</sup>, Alan G. Green<sup>1</sup>, Stewart Greenhalgh<sup>1</sup>, Lasse Rabenstein<sup>1</sup>, Joseph Doetsch<sup>4</sup>, Wolfgang Kinzelbach<sup>3</sup>, Esben Auken<sup>5</sup>, Peter Mikkelsen<sup>5</sup>, Nikolaj Foged<sup>5</sup>, Bashali Charles Jaba<sup>6</sup>, Gomotsang Tshoso<sup>6</sup>, and Onkgopotse Ntibinyane<sup>6</sup>

### ABSTRACT

The Okavango Delta is a huge alluvial megafan in northwestern Botswana. Despite numerous geologic, geochemical, geophysical, and hydrologic investigations over the past half-century, the sedimentary units underlying the delta are largely unknown. To address this issue, helicopter transient electromagnetic data (HTEM) have been collected across the entire delta and coincident ground-based electrical resistance tomographic (ERT) and transient electromagnetic (TEM) data have been acquired at two locations, one along the delta's western margin and one in its north-central region. Inversions of the HTEM data have yielded three-layer resistivity models in which a relatively homogeneous conductive layer is sandwiched between two resistive layers. The three-layer HTEM model is reproduced in models obtained from independently and jointly inverting the ground-based data. The conductive layer's low resistivities and depths to its upper and lower boundaries are practically

equal in the HTEM and ground-based models. Resistivities of the upper resistive layer are similar in the various models, with the ground-based estimates being somewhat higher than those of the HTEM model at one site and somewhat lower at the other site. For the basal resistive layer, it can only be concluded that its resistivity must be substantially higher than that of the overlying conductive layer. An interpretation of the HTEM and ground-based resistivity models in the delta's north-central region, appropriately constrained by the surface geology, high-resolution seismic refraction-reflection models, and borehole logs suggests the following structure: basement overlain at progressively shallower depths by freshwater-saturated sand and gravel that represent the remnants of a Paleo Okavango Megafan, saline-water-saturated sand, and lacustrine clay originally deposited in Paleo Lake Makgadikgadi, and freshwater-saturated megafan and fluvial sediments of the current Okavango Delta.

Manuscript received by the Editor 3 January 2014; revised manuscript received 9 April 2014; published online 21 July 2014.

<sup>1</sup>ETH Zürich, Institute of Geophysics, Zürich, Switzerland. E-mail: philipmeier@tbwil.ch; joel.podgorski@erdw.ethz.ch; alan.green@erdw.ethz.ch; stewart.greenhalgh@erdw.ethz.ch; lasse.rabenstein@erdw.ethz.ch.

<sup>2</sup>Uppsala University, Department of Earth Sciences, Uppsala, Sweden; formerly at ETH Zürich, Institute of Geophysics, Zürich, Switzerland. E-mail: thomas.kalscheuer@geo.uu.se.

<sup>3</sup>ETH Zürich, Institute of Environmental Engineering, Zürich, Switzerland. E-mail: kgotlhang@gmail.com; kinzelbach@ifu.baug.ethz.ch.

<sup>4</sup>ETH Zürich, Institute of Geophysics, Zürich, Switzerland; formerly at Aarhus University, Department of Geoscience, Aarhus C, Denmark. E-mail: joseph.doetsch@sccer-soe.ethz.ch.

<sup>5</sup>Aarhus University, Department of Geoscience, Aarhus C, Denmark. E-mail: esben.auken@geo.au.dk; peter.mikkelsen@geo.au.dk; nikolaj.foged@geo.au.dk.

<sup>6</sup>Department of Geological Survey, Lobatse, Botswana. E-mail: bcjaba@yahoo.com; gtshoso@gov.bw; ontibinyane@gov.bw.

© 2014 Society of Exploration Geophysicists. All rights reserved.

## INTRODUCTION

The Okavango Delta is one of the world's great inland alluvial megafans, covering an area of about 40,000 km<sup>2</sup> (McCarthy, 2006, 2013). Situated at the terminus of the endoreic Okavango River along the northwestern margin of the Kalahari Desert (Figure 1), the delta is a vast perennial water body with a semiarid climate that provides exceptional conditions for diverse flora and fauna to flourish.

An average of ~10 km<sup>3</sup>/year of river water flows into the delta, and there is an average of ~6 km<sup>3</sup>/year of direct rainfall (McCarthy, 2006). However, water influx varies enormously both seasonally and from year to year. Permanent water within the Panhandle and other parts of the delta covers ~3300 km<sup>2</sup>, whereas another 3300–10,400 km<sup>2</sup> of land is inundated on a seasonal basis (McCarthy, 2013). Peak flooding near the Panhandle (Figure 1) occurs in late April to early May, and then slow downstream propagation causes flooding at the delta's southeastern extremity three to four months later. Very little water exits the delta in rivers and in the subsurface. Instead, most of the water (~95%) is released to the atmosphere via evapotranspiration. The transpiration of groundwater by vegetation along the edges of islands precipitates substantial volumes of salt at the surface and within the shallow subsurface (McCarthy, 2006, 2013). It has been postulated that density instabilities created by the high salt concentrations cause saline plumes to sink into deep parts of the delta's groundwater system (McCarthy and Ellery, 1994; Gieske, 1996; Milzow et al., 2009).

The delta lies within a ~150-km-wide asymmetric graben bounded by normal faults (Figure 1) presumed to represent a southwestward extension of the East African Rift System (Scholz et al., 1976; Grey and Cooke, 1977; Cooke, 1980; Modisi et al., 2000;

McCarthy, 2006, 2013). Active seismicity (Fairhead and Girdler, 1971; Reeves, 1972; Hutchison and Midgley, 1973; Scholz et al., 1976), the fresh character of the faults, and displacements of relatively young sedimentary units demonstrate that extensional tectonism is ongoing. Indeed, water flow paths changed in the early 1950s following an M 6.7 earthquake (Hutchison and Midgley, 1973). Over longer time scales, tectonic activity has clearly influenced the channel morphology within the delta and near its borders, in particular along the Kunyere-Thamalakane fault zone (Figure 1; McCarthy et al., 1993; McCarthy, 2006, 2013). Moreover, the entire Kalahari Basin of southern Africa, which encompasses the Okavango Delta, has been subjected to numerous phases of tectonism (Burke and Gunnell, 2008) that resulted in multiple redirections of major river systems (Thomas and Shaw, 1991; Moore and Larkin, 2001; McCarthy, 2006, 2013; Burrough et al., 2009; Moore et al., 2012). The varying courses of these rivers had a significant impact on sedimentation within the region now occupied by the delta, such that the local hydrologic and depositional conditions likely varied from fluvial to lacustrine, megafan, and aeolian. Because high evaporation rates characterize this region of Africa, Podgorski et al. (2013b) have suggested that some lacustrine units were likely deposited in saline lakes.

Today, the Okavango Delta is a massive alluvial fan underlain by sediments that comprise the main aquifers. Considering its tectonic environment, the surface topography is surprisingly subdued, with only a 60-m decrease in elevation over the 250-km distance between the Panhandle and the Kunyere-Thamalakane fault zone (Figure 1; Gumbrecht et al., 2005). In contrast, limited borehole data near the Panhandle and several seismic data sets elsewhere within the delta suggest that basement depth increases from 45 to 360 m over the same distance range (Podgorski et al., 2013b). The sedimentary section beneath the central part of the delta is not well known. There is no information on the sediments intersected by the boreholes near the Panhandle, and no borehole has penetrated the entire sedimentary section within the heart of the delta. Based on extensive drilling at its southeastern end (MMEWR, 2004) and a single drilling on Thata Island east of Jao in Figure 1 (Bauer et al., 2006), sediments representing the past depositional conditions at these locations range from sand, clayey sand, and sandy clay to thick sequences of clay (Milzow et al., 2009; Podgorski et al., 2013b).

Electrical and electromagnetic methods offer efficient means for studying the hydrogeology and lithologies of the Okavango Delta (MMEWR, 2004; Sattel and Kgotlhang, 2004; Bauer et al., 2006; Shemang and Molwalefhe, 2009; Bauer-Gottwein et al., 2010). Because electrical resistivity is generally a good proxy for water saturation, salinity, and lithology, these methods have long been used for investigating aquifer systems worldwide (e.g., Fitterman and Stewart, 1986; Albouy et al., 2001; Danielsen et al., 2007). Depending on the local situation, decreasing electrical resistivity is usually evidence for increasing water saturation, and/or salinity, and/or clay content. To take advantage of the cost-effective nature of airborne electromagnetic methods for rapidly investigating hydrological parameters and lithologies beneath large areas, HTEM data were recorded across the Okavango Delta under contract to the Botswana Department of Geological Survey. Podgorski et al. (2013b) present an evolutionary model for the Okavango Delta based on a highly simplified version of the regional resistivity model derived from the HTEM data (to highlight the basic three-layer nature of the model to a general geoscience readership, resistivities were represented by

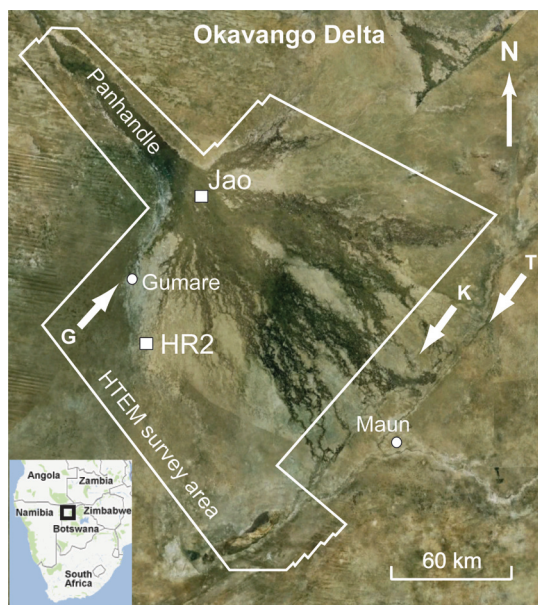


Figure 1. Location of Okavango Delta. Polygon: area of regional helicopter transient electromagnetic (HTEM) survey. Squares: HR2 and Jao ground-based field sites. Large oblique arrows: main faults (G–Gumare; K–Kunyere; and T–Thamalakane). The Okavango River flows through the Panhandle into the delta. Satellite image from Google Earth (© 2012 Google). Inset: southern Africa with box marking the Okavango Delta region.

just three clusters of values with a single color for each cluster) and diverse other geoscience information.

To supplement the information contained in the HTEM models and guide the associated interpretation, we have processed and inverted ground-based electrical resistance tomographic (ERT), transient electromagnetic (TEM), and high-resolution seismic refraction–reflection data recently collected at two field sites within the Okavango Delta (Figures 1 and 2). Results of the seismic surveys have been reported by Reiser et al. (2014). Here, we begin by introducing the HTEM surveys and presenting the regional HTEM resistivity model in a non-clustered form for the first time; the HTEM resistivity model provides a basis for understanding the results of inverting the ground-based data. After describing the conditions and data acquisition at the two field sites, we review our processing and inversion strategies and assess the HTEM and ground-based ERT and TEM models. Finally, we present an integrated interpretation of the HTEM and ground-based resistivity models constrained by coincident high-resolution seismic reflection images and tomographic P-wave velocity models, surface geology, and limited borehole information (Reiser et al., 2014).

### HTEM SURVEYS AND REGIONAL RESISTIVITY MODEL

Three HTEM surveys were conducted within the Okavango Delta: a regional survey of 15,000-line km covering the whole delta with a nominal line spacing of 2 km and two high-resolution surveys covering smaller areas with a much closer nominal line spacing of 50 m. One high-resolution survey (HR1) was flown across a  $5 \times 5$  km<sup>2</sup> area approximately centered on the Thata Island borehole and the second (HR2) was flown across a  $5 \times 7$  km<sup>2</sup> area along the western edge of the delta. Because the acquisition parameters and processing and inversion steps applied to the HTEM data are described in detail by Podgorski et al. (2013a), they will not be described here.

The quality of the HTEM data is exceptionally high, primarily because of the low noise environment (few settlements and no major overhead cables, pipelines, or other major infrastructure) and strong contrasts between the electrically resistive units (i.e., freshwater, dry and freshwater-saturated sand, and basement) and electrically conductive ones (i.e., saline-water-saturated sand and clay). Figure 3 shows constant-depth resistivity slices extracted from a laterally constrained inversion (LCI) (Auken and Christiansen, 2004) model of the regional HTEM data set that is characterized by three principal layers. A variably thick heterogeneous surface to near-surface layer of moderate to high resistivities overlies a low-resistivity (i.e., electrically conductive) layer throughout most of the delta. Beneath the conductive layer in the northwestern half of the surveyed area is an arcuate-shaped high-resistivity unit (Figure 3f). The same basic three-layered resistivity structure is observed in spatially constrained inversions (SCI) (Viezzoli et al., 2008) of the high-resolution HTEM data sets recorded at HR1 and HR2.

### SITE CONDITIONS AND ACQUISITION OF GROUND-BASED DATA

A variety of environmental and logistical issues limited our options for acquiring ground-based data within the Okavango Delta. As examples, the entire delta is the world's largest Ramsar Site (Kabbi, 1997) and a proposed UNESCO World Heritage Site, and much

of its dry land lies within the protected Moremi Game Reserve. One of our investigation sites was situated within the high-resolution HTEM survey area HR2 near the western edge of the delta. This site, which lies outside the wild animal barrier, was accessible by land-based vehicles. ERT and TEM data were recorded along a single line (line 1 in Figure 2a), along which elevations varied by only  $\pm 2$  m from the local mean value as determined by differential GPS measurements. The recording line transected open land with predominantly dry sand and intermittent clay at the surface. Soft wet ground was observed in the vicinity of the line.

The second site was at Jao on Jedibe Island in the north-central part of the delta. Jao is a rare location within the delta that is sparsely populated; most of the delta is uninhabited. Because there are no land-based vehicles on the island, the heavy geophysical equipment had to be manually deployed and retrieved. The HTEM

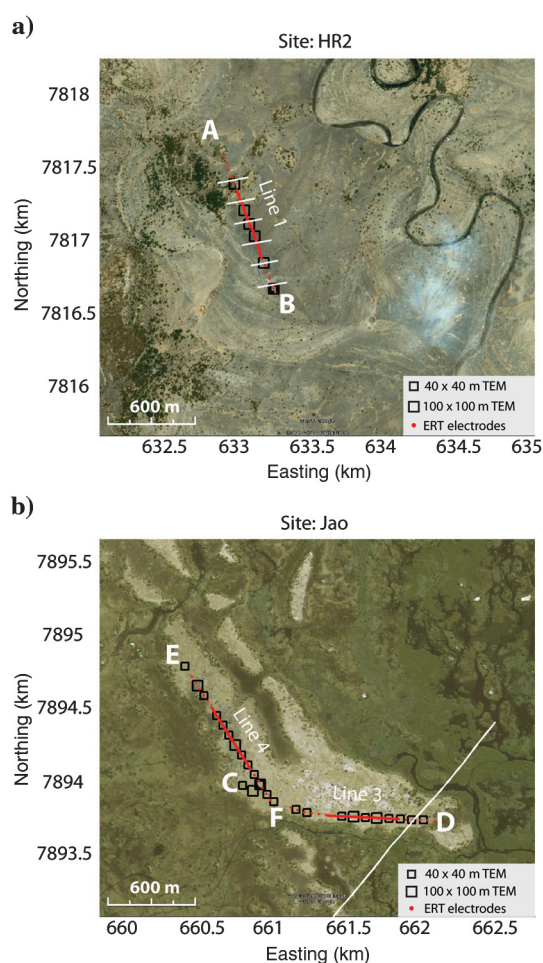


Figure 2. Ground-based survey lines at the (a) HR2 and (b) Jao field sites showing locations of the ERT electrodes (closely spaced red dots) and TEM soundings (black squares, the sizes of which are not proportional to loop sizes). Small white lines in (a) are cross sections of spatially constrained high-resolution HTEM model displayed in Figure 7 (cross sections coincide with flight lines). Oblique white line in (b) is location of laterally constrained regional HTEM model displayed in Figure 10 (cross section coincides with flight line). A–B, C–D, and E–F at the ends of ERT/TEM lines 1, 2, and 3 also define the limits of the seismic lines described by Reiser et al. (2014). Satellite images from Google Earth (© 2011 Google).

data recorded across the island are somewhat atypical for the delta in that they do not detect a relatively thick resistive layer at the surface (this cannot be discerned at the scale of Figure 3). Other aspects of the data acquired across the island are representative of the entire HTEM data set (i.e., they detect the presence of a thick conductive layer and an underlying resistive layer). Although measurements were made along two lines (Figure 2b), we will concentrate on the highest quality data acquired along the east–west-trending line 3. Elevations along this line varied by only  $\pm 1$  m from the local mean value, and relatively compact sand, clayey sand, and salty sand were observed at the surface.

A SYSCAL multichannel resistivity recording system was used to acquire the ERT data. Along each line, 96 electrodes were deployed with a uniform 5-m spacing. To increase penetration depth, additional current electrodes were deployed on either side of the main electrode array with a uniform 50-m spacing at distances between 250 and 500 m from the centers of the lines. The data were recorded using 1924 dipole-dipole configurations with multiple dipole lengths and 3550 gradient configurations. The far-offset measurements contributed an additional 404 data points. Reciprocal data were recorded for all configurations involving only the central 96 electrodes. At dry sandy locations, soaking the ground with water in the immediate vicinity of the current electrodes was usually necessary to decrease contact resistances. For the same purpose, we used five closely spaced electrodes connected in parallel at each of the far-offset locations.

Our ground-based TEM data were acquired using the WalkTEM instrument (Nyboe et al., 2010), which was precalibrated at the Danish TEM-test site (Foged et al., 2013). Soundings were made using central-loop configurations with  $40 \times 40$  m and  $100 \times 100$  m transmitter loops and 1- and 8-A current pulses for low- and high-moment sources, respectively. Vertical magnetic field transients were recorded using receiver coils with effective areas of  $105 \text{ m}^2$

for the low-moment sources and  $4200 \text{ m}^2$  for the high-moment sources. The transient decays were recorded over a 2.2–8800- $\mu\text{s}$  time range with expected investigation depths down to 200 m (see Table 4 in Podgorski et al. [2013a] for further details on the WalkTEM system and TEM acquisition parameters). A total of 33 central-loop TEM soundings (i.e., data sets) were recorded along three lines (Figure 2).

## INVERSION STRATEGIES AND ESTIMATING RELIABILITY

### Inversions of ERT data and resolved parts of the inverted models

We applied smoothness constraints in the 2D inversions of the ERT data using the RES2DINV code (Loke and Barker, 1996; Loke, 1997) and followed Oldenburg and Li's (1999) recommendation in assuming that model parameters were relatively well resolved at locations where depth of investigation (DOI) indices were  $< 0.2$ .

### Inversions of TEM data

To compare the results of inverting multiple ground-based TEM soundings recorded along each line with the results of inverting nearby HTEM soundings, we used the same LCI/SCI code. Models determined from simple 1D inversions (e.g., Jupp and Vozoff, 1975) of TEM data typically comprise a series of layers defined by layer resistivities and thicknesses (or depths). For TEM soundings located along a profile, the individual 1D models can be linked to each other by applying lateral constraints to the model parameters (Auken and Christiansen, 2004). This is achieved by incorporating a common objective function in the inversion process. The lateral constraints are scaled according to the distances between the 1D models (Christiansen et al., 2007) as

$$C_l = (C_r - 1) \left( \frac{d}{d_r} \right)^{\frac{1}{2}} + 1, \quad (1)$$

where  $C_l$  is the lateral constraint,  $C_r$  is a reference constraint,  $d$  is the distance between individual measurements, and  $d_r$  is a reference distance:  $C_r$  and  $d_r$  are the parameters to adjust. Because constraints provided by the data invariably decrease with depth, lateral constraints are usually chosen to increase with depth. Values of  $C_l$  close to 1 impose strong coupling between neighboring models, whereas larger values impose weaker coupling. As an example,  $C_l = 1.1$  should ensure that parameters of neighboring models have mutual deviations of only  $\sim 10\%$ . The result of applying the LCI code to multiple TEM soundings recorded close together along a line is a pseudo-2D resistivity section composed of laterally constrained 1D models.

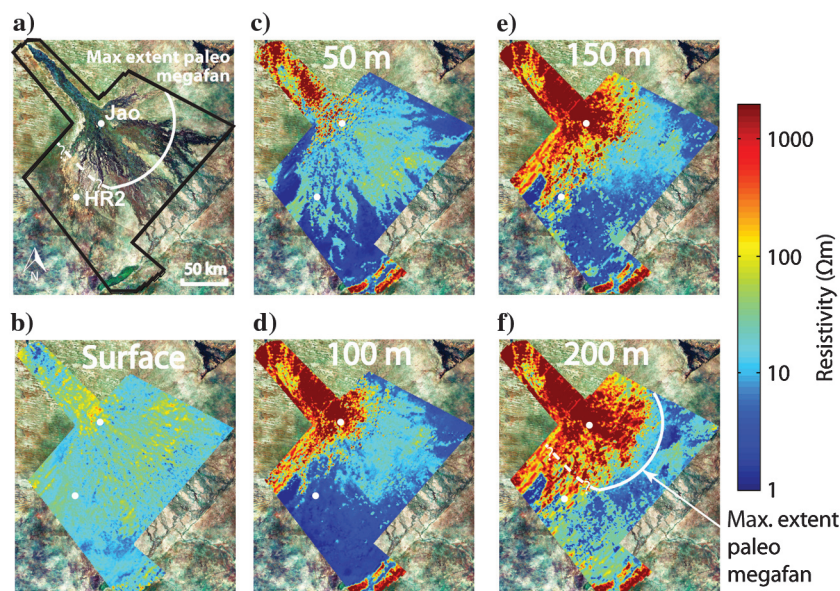


Figure 3. (a) Okavango Delta and HR2 and Jao field sites. (b-f) Resistivity model derived from a laterally constrained inversion of the regional HTEM data depicted as slices at different depths below the surface. Justification for the paleo megafan is briefly provided in the text and fully explained in Podgorski et al. (2013b).

## Joint inversions of ERT and TEM data

We also jointly invert the coincident ERT and TEM data using the mutually and laterally constrained inversion (MCI/LCI) scheme of Christiansen et al. (2007). In addition to imposing lateral constraints, mutual constraints between parameters of the ERT and TEM models are enforced by the MCI/LCI scheme. In this way, poorly determined model parameters of one method may be constrained by better determined parameters of the other.

## Reliability of LCI and MCI/LCI models

To determine which parts of LCI and MCI/LCI models are stable or well determined, a standard deviation factor (STDF) is computed for each model parameter (Auken et al., 2005). The STDF is derived from the diagonal elements of the linearized posterior model covariance matrix. Theoretically,  $STDF = 1.0$  for a parameter free of error.  $STDF = 1.1$  indicates that a parameter has 10% possible variability or error. According to Auken et al. (2005), model parameters are well determined if  $STDF < 1.2$ , reasonably well determined if  $STDF < 1.5$ , poorly determined if  $STDF < 2$ , and largely undetermined if  $STDF > 2$ .

## PROCESSING AND INVERSION OF THE GROUND-BASED DATA

In this section, we illustrate the results of applying our processing and inversion strategies using ERT and TEM data recorded along line 1 at the HR2 investigation site.

### Electrical resistance tomographic data

Editing the data was the first processing step. Reciprocal ERT measurements that differed by more than 5% were automatically discarded. Unreliable measurements seen as outliers on pseudosections or identified by large misfits with model predictions estimated from preliminary inversions were also eliminated. Based on the majority most of reciprocal values, uncertainties of 3% were allocated to data points acquired with the principal 96-electrode array. A larger uncertainty of 5% was assumed for data generated by the offset current electrodes. After editing and assigning uncertainties, numerous smoothness-constrained 2D inversion models were computed for each line of data.

Figure 4a shows a model derived from applying the RES2DINV code to line 1 data. Dipole-dipole data in pseudosection form with one subplot for each dipole length ( $a = 5 - 20$  m) are displayed in Figure 4b, and corresponding pseudosections computed for the model in Figure 4a are presented in Figure 4c. Matches between the observed and computed gradient data are comparable to those shown for the dipole-dipole data. Misfits between the observed and calculated data have an rms deviation of 5.4%.

Like the HTEM resistivity model of Figure 3, the model in Figure 4a contains a surface resistive unit overlying a conductive one. The thickness of the surface resistive unit varies between 20 and 35 m. Its resistivity lies mainly in the 300–400  $\Omega\text{m}$  range with minor heterogeneous features having resistivities as low as 50  $\Omega\text{m}$  and as high as 1000  $\Omega\text{m}$ . Resistivities of the conductive unit are uniformly  $< 10$   $\Omega\text{m}$  with large regions of 2–3  $\Omega\text{m}$ . Although a lower resistive layer is required by the ERT data, in particular for the long-offset recordings, the DOI analysis (white line in Figure 4a)

indicates that neither its resistivity nor its depth is resolved in the inverted models.

## TEM data

After eliminating excessively noisy recordings using the same procedures as described for the HTEM data in Podgorski et al. (2013a), the TEM data (i.e., the  $\partial B_z / \partial t$  (time rate of change of the secondary vertical magnetic field) and  $\rho_a$  (apparent resistivity) transients) were averaged and uncertainties set to the corresponding standard deviations plus a base value of 3%. Subsequently, the averaged sounding curves were judiciously edited, the guiding rule being that the sounding curves should be smooth without sudden fluctuations (Podgorski et al., 2013a). Special attention was given to the earliest and latest time gates because the induced voltages occasionally exceeded the input voltage range of the instrument in the earliest gates and decreasing signal-to-noise ratios led to relatively noisy transient voltages in some later gates. Representative data after editing are shown by the crosses in Figure 5d.

All TEM soundings recorded along line 1 are very similar, suggesting predominantly 1D conditions at this site. The observed data are explained by the model in Figure 5a to within 1.7% rms (Figure 5b). Average resistivities of the progressively deeper layers in Figure 5a are approximately 91, 6, 3, and 101  $\Omega\text{m}$ , and

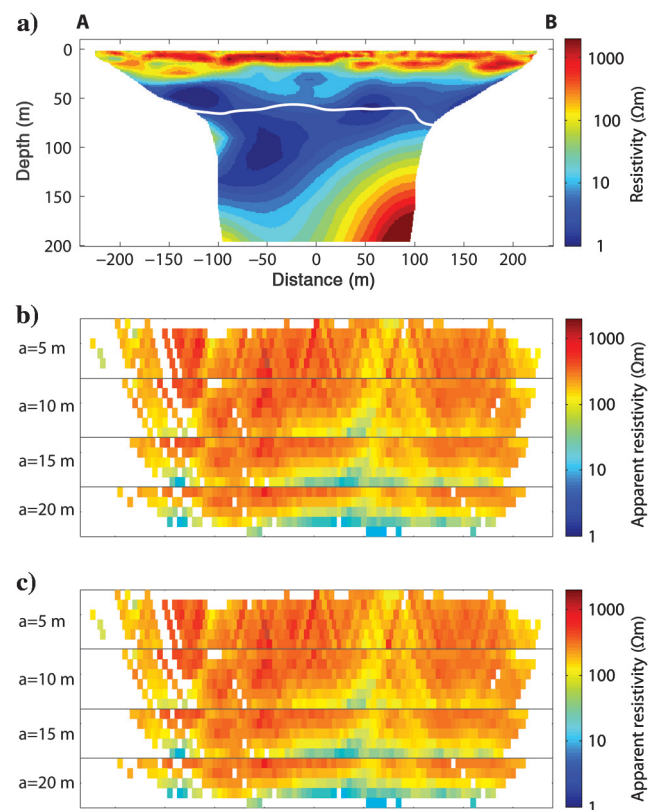


Figure 4. HR2, line 1 (line location is shown in Figure 2a): results of smoothness-constrained 2D inversion of ERT data showing (a) derived 2D resistivity model, (b) pseudosections of observed dipole-dipole data subset for different dipole spacings, (c) predicted pseudosections of the derived resistivity. Depth of investigation (DOI) indices are mostly  $> 0.2$  below the white line in (a). The rms difference between observed and model-predicted data is 5.4%.

average interface depths are approximately 29, 51, and 141 m. STDF values in Figure 5c indicate that all parameters are well determined except the resistivity of the deepest layer, which must be greater than the resistivity of the overlying layer but is otherwise largely undetermined.

### Joint inversion

Figure 6a shows the results of jointly inverting the ERT and ground-based TEM data recorded along line 1 using the MCI/LCI code (note that the ERT data influence the inverted model only between distances  $-220$  and  $+220$  m). Five layers were required to produce acceptable rms differences between the observed and model-predicted data. The rms deviations in Figure 6b for the TEM data (blue dots) are uniformly  $\leq 2.5\%$ , a little larger than the values for the individual LCI TEM inversion (Figure 5b). For the ERT data (red dots), the rms deviations are mostly in the  $2.5\%$ – $7.5\%$  range. STDF values in Figure 6c suggest that most of the depths and resistivities are well determined to reasonably well determined. A notable exception is again the resistivity of the basal layer.

Simple comparisons demonstrate that the upper and lower parts of the jointly inverted model of Figure 6a resemble the upper part of the ERT model in Figure 4a and the lower part of the TEM model in Figure 5a, respectively. Nevertheless, the combined  $\sim 29$ -m mean thickness of the resistive upper two layers of Figure 6a is almost the

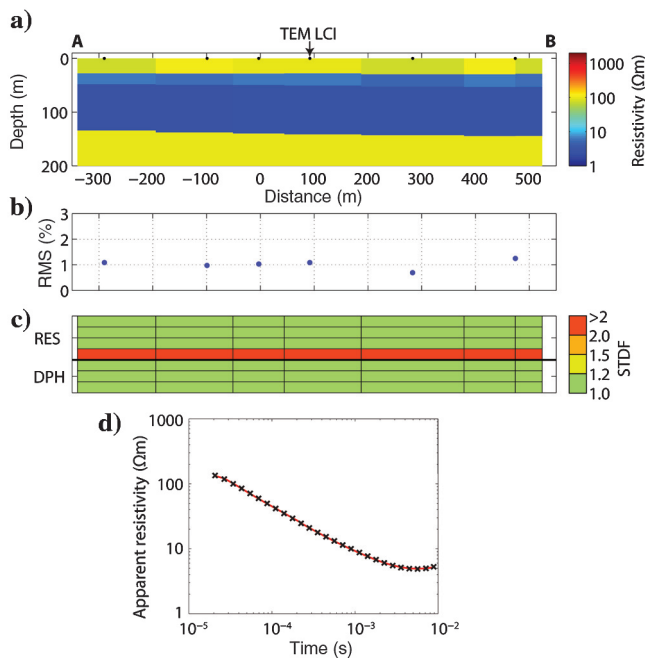


Figure 5. HR2, line 1: results of laterally constrained 1D inversion of ground-based TEM data showing (a) derived pseudo-2D resistivity model, (b) rms differences between observed and model-predicted data, (c) standard deviation factors (STDF) for resistivities (RES) of layers 1–4 (upper four horizontal layers of boxes) and depths (DPH) to the top of layers 2–4 (lower three horizontal layers of boxes), and (d) data (crosses) and model response (red line) for a typical TEM site [location shown by the arrow in (a)]. For the inversion shown in this figure,  $d_r$  in equation 1 is 100 m,  $C_r - 1$  is 5.0 and 0.1 for the resistivities in the upper two and lower two layers, respectively, and  $C_r - 1$  is 0.17, 0.10, and 0.04 for the depths to the increasingly deeper layer boundaries.

same as the mean thickness of the resistive uppermost layer of Figure 5a. The depth to the top of the resistive basal layer in Figure 6a is about 136 m. Applications of the MCI/LCI code using a wide variety of starting models indicate that this layer can be at any depth in the 120–148-m range and that it must have a resistivity of at least  $15 \Omega\text{m}$  to explain the small but consistent increases in apparent resistivities in the late time gates (e.g., Figure 5d).

## GROUND-BASED AND HELICOPTER RESISTIVITY MODELS

### HR2 site

A comparison of the LCI model derived from the ground-based TEM data acquired along line 1 with cross sections extracted from the SCI model derived from the high-resolution HTEM data recorded across HR2 is presented in Figure 7. Note how the resistivity and depths to the top and bottom of the conductive layer are very similar ( $<20\%$  relative deviation) in the two models. By compari-

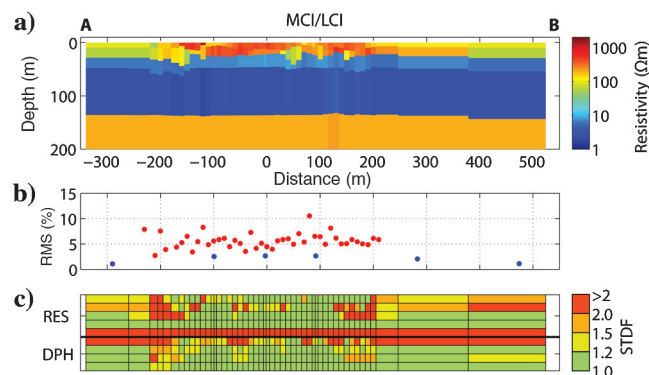


Figure 6. HR2, line 1: results of mutually and laterally constrained inversion of ERT and TEM data showing (a) derived pseudo-2D resistivity model, (b) rms differences between observed and model-predicted data (red dots: ERT data; blue dots: TEM data), and (c) standard deviation factors (STDF) for resistivities (RES) of layers 1–4 (upper four horizontal layers of boxes) and depths (DPH) to the top of layers 2–4 (lower three horizontal layers of boxes).

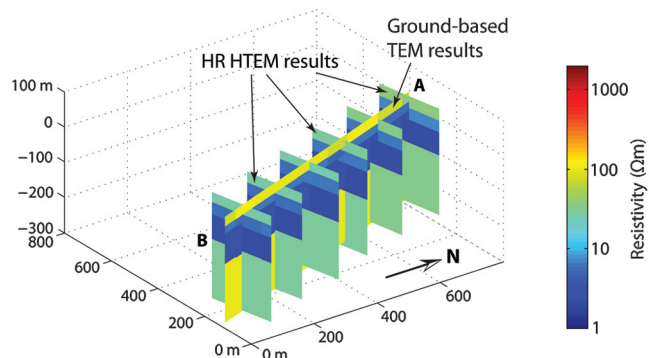


Figure 7. HR2, line 1: pseudo-2D resistivity model derived from a laterally constrained inversion of ground-based TEM data versus cross sections extracted from a pseudo-3D model derived from a spatially constrained inversion of the high-resolution HTEM data (for locations of lines see Figure 2a).

son, resistivities of the upper and basal resistive layers in the ground-based model are somewhat higher than those in the HTEM model ( $\sim 100 \Omega\text{m}$  in the ground-based model versus  $\sim 30 \Omega\text{m}$  in the HTEM model). Based on the ERT model of Figure 4a and the jointly inverted ERT/TEM model of Figure 6a, it is highly likely that near-surface resistivities are even higher than those inferred from the ground-based TEM data. Multiple forward modeling computations and inversions demonstrate that the resistivity of the lower resistive layer is no better determined in the HTEM model than in the ground-based models.

Considering the relatively simple 1D character of the ground-based and HTEM models in Figure 7, we calculated horizontally averaged resistivity-depth sections for all models. Plots of these sections in Figure 8 highlight the similarities and differences between the models derived from the different data sets. The ERT model based on measurements every 5 m provides the highest resolution and most reliable resistivity information for the top  $\sim 29$  m of the site. Average resistivities in this shallow region of the smoothness-constrained ERT and jointly inverted models are markedly higher than those in the models based on the ground-based TEM data alone and the HTEM data. It is noteworthy that the average 2–3- $\Omega\text{m}$  resistivities of the main part of the conductive layer and the average  $\sim 29$ -m depth to its upper surface are consistent in all models. Although a lower resistive layer is required to explain the long-offset ERT data, the ERT model does not resolve its depth or resistivity. The near coincidence of the depth to the lower resistive layer (i.e., base of the conductive layer) in the average ground-based TEM and HTEM models (see the lower parts of the models in Figure 8) and the associated low STDF values in Figures 5c and 6c suggest that this depth has been reliably determined. In contrast, the resistivity of the lower resistive layer is only constrained to be greater than about 15  $\Omega\text{m}$ .

### Jao site

The processing and inversion strategies described for the ground-based ERT and TEM data recorded at HR2 were applied to the equivalent data acquired at Jao. Despite the markedly different resistivities in the upper 50 m of ground at the two sites, most of the processing and inversion parameters optimized for the HR2 data were found to be suitable for the Jao data. Results of inverting the ground-based data collected along line 3 at Jao are summarized in the smoothness-constrained 2D ERT model in Figure 9, the LCI TEM model in Figure 10, and the horizontally averaged resistivity-depth sections based on all models in Figure 11.

Our 2D ERT model for line 3 (Figure 9) reveals horizontal layering with apparently only minor lateral heterogeneity. A near-surface conductive layer with resistivities of 1–9  $\Omega\text{m}$  is separated from a zone of increasing resistivity at about a 30-m depth. It is not clear from our ERT data alone whether the relatively gradual nature of the resistivity increase between 30- and 50-m depth in Figure 9 represents conditions in the subsurface or is an artifact created by the smoothness constraints used in the inversion process. Because the DOI indices are  $>0.2$  below  $\sim 50$  m depth, the resistivities

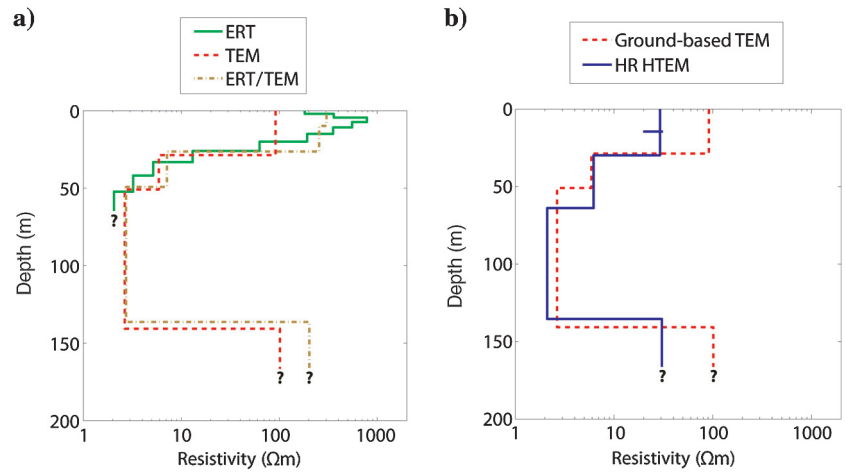


Figure 8. HR2, line 1: (a) horizontal averages of models derived from smoothness-constrained 2D inversion of ERT data (solid green line), laterally constrained inversion of ground-based TEM data (dashed red line), and mutually and laterally constrained inversion of ERT and TEM data (dashed-dotted brown line). (b) Horizontal averages of models derived from laterally constrained inversion of ground-based TEM data (dashed red line) and spatially constrained inversion of high-resolution HTEM data (solid blue line).

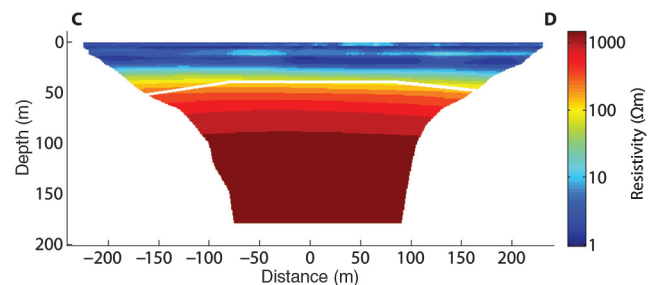


Figure 9. Jao line 3 (line location is shown in Figure 2b): resistivity model derived from a 2D smoothness-constrained inversion of ERT data. Depth of investigation (DOI) indices are mostly  $>0.2$  below the white line. The rms difference between observed and model-predicted data is 4.8%.

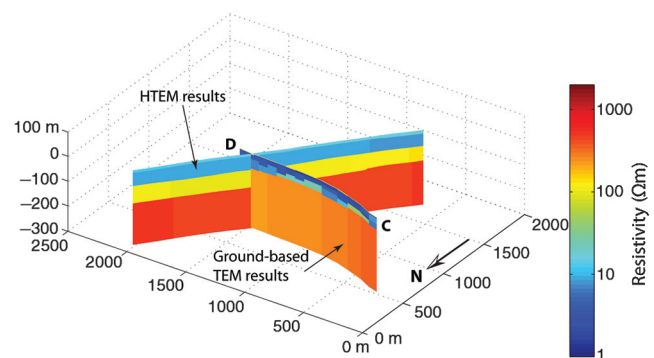


Figure 10. Jao line 3: pseudo-2D resistivity model derived from a laterally constrained inversion of ground-based TEM data versus a pseudo-2D resistivity model derived from a laterally constrained inversion of the crossing regional HTEM data (for locations of the lines, see Figure 2b).

of the lower resistive layer are not well determined. The near absence of heterogeneity in the upper conductive layer in Figure 9 is to some extent a consequence of using dark blue to represent the 1–9- $\Omega\text{m}$  range of resistivities (for consistency, we used the same resistivity color scale in all figures). The ERT horizontally averaged resistivity–depth section in Figure 11 indicates that there are some variations within this resistivity range at Jao.

The first-order conductive–resistive layering observed in the 2D ERT model of Figure 9 is reproduced in the LCI TEM model of Figure 10 and the MCI/LCI model of the two data sets (not shown here because of its close resemblance to the LCI TEM model). Resistivities of  $<9 \Omega\text{m}$  in the near-surface 30-m-thick conductive layer are practically the same in all three models. However, a very thin ( $<4 \text{ m}$ ) shallow resistive unit (represented by the thin orange line along the top of the ground-based TEM model in Figure 10) is required to explain early time-gate data on all TEM data recorded at Jao. These units in the ground-based TEM model have thicknesses of  $\sim 2 \text{ m}$  and resistivities of  $>100 \Omega\text{m}$ , but these values are not well constrained by the data. Their absence in the ERT model is most likely a consequence of the 5-m-electrode spacing used for collecting the ERT data. The boundary between the near-surface conductive layer and the deep resistive layer is represented in parts of the ground-based TEM model by a 10- to 30-m-thick unit with intermediate resistivities, offering support for the authenticity of the transition zone at 30–50-m depth in the ERT model. According to the STDF analysis (not shown), the resistivities and depths to the lower boundaries of the conductive layer and transitional zone are well determined to reasonably well determined.

The distribution of resistivities within the transition zone is somewhat inconsistent in the ERT and TEM models. In the 2D ERT model (Figure 9), the transition zone is represented by a laterally uniform gradual increase in resistivity, whereas in the LCI TEM model (Figure 10), it appears as laterally discontinuous blocks of constant resistivity. These discrepancies could be influenced by shortcomings in the 2D and pseudo-2D approaches we have employed. Both data sets are undoubtedly affected by current channeling in 3D heterogeneous conductive units in the shallow subsurface. These effects are likely to be different for the ERT and TEM data sets. We also note that the TEM data may be contaminated by lateral

heterogeneity caused by the high resistivities of freshwater in channels several tens of meters south of the recording line (Figure 2b).

At the intersection of the ground-based TEM and regional HTEM models, the  $\sim 50\text{-m}$  thickness of the near-surface conductive layer matches, but its resistivity in the ground-based TEM model is somewhat lower than that in the HTEM model (Figure 10). In contrast, the resistivity of the immediately underlying region in the ground-based TEM model is noticeably higher than that in the HTEM model. Other differences between the models are the higher level of lateral heterogeneity in the former than in the latter, and the presence of a discrete resistivity increase at  $\sim 130\text{-m}$  depth in the HTEM model that is not required by the ground-based data. Dissimilarities between the two models are partially due to the much larger footprint and more powerful transmitter of the HTEM system than those of the WalkTEM instrument; because the flight line only crosses a narrow portion of the island at its eastern edge (Figure 2b), a significant proportion of the near-surface footprint of the HTEM system covers fresh open water (partly covered by papyrus) with relatively high resistivity.

A near-surface conductive layer with resistivities  $\leq 9 \Omega\text{m}$  and a deeper resistive layer are featured in all horizontally averaged sections in Figure 11. Considering the footprint issue, the  $\sim 65\text{-m}$  thickness and  $\sim 9\text{-}\Omega\text{m}$  resistivity of the conductive layer in the average HTEM model are compatible with the average ground-based models in which a  $\sim 30\text{-m}$ -thick layer of 1–4- $\Omega\text{m}$  resistivity overlies a  $\sim 25\text{-m}$ -thick transitional layer of  $\sim 20\text{-}\Omega\text{m}$  resistivity. Although the resistivity of the lowermost resistive layer(s) in the models is not well constrained, sensitivity tests based on multiple forward modeling and inversions suggest that it must be at least 25  $\Omega\text{m}$ .

## DISCUSSION

### Local hydrogeologic and geologic models

Resistivity models derived from the ground-based ERT and TEM data are generally compatible with the HTEM models (Figures 7, 8, 10, and 11). As well as providing supporting evidence for the resistive–conductive–resistive layering at HR2 and the conductive–resistive layering at Jao, the ground-based inversions yield additional details and refinements to the resistivity and depth estimates.

Unfortunately, the resistivities of the lowermost resistive layer at the two sites are not well determined by any of the ground-based and HTEM models. Probable minimum resistivities are 15  $\Omega\text{m}$  at HR2 and 25  $\Omega\text{m}$  at Jao. However, for the majority of plausible ground-based models they are  $>100 \Omega\text{m}$  at HR2 and  $>200 \Omega\text{m}$  at Jao. In the regional HTEM model (Figure 3e and 3f), they mostly range from 100 to 2000  $\Omega\text{m}$  throughout the northern part of the delta.

For our interpretation of the ERT and TEM models we take advantage of (1) direct visual observations of the surface sediments and water-saturation conditions at the investigation sites, (2) coincident high-resolution seismic refraction–reflection models (for locations, see Figure 2; Reiser et al., 2014), (3) basement depths encountered in a limited number of boreholes (Podgorski et al., 2013b), (4) salinity profiles of water in waterwells at various locations within

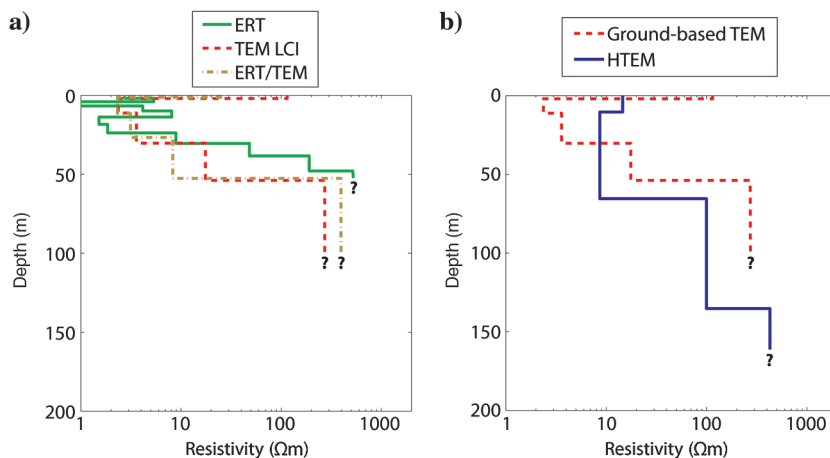


Figure 11. As for the caption to Figure 8, but for Jao line 3 and the laterally constrained regional HTEM model that crosses this line.

the delta (T. Preston, personal communication, 2011), and (5) hydrogeologic and lithological information determined from numerous boreholes at the southeastern end of the delta (MMEWR, 2004; Milzow et al., 2009) and from one borehole on Thata Island east of Jao (Bauer et al., 2006). Simple models that summarize key details of the ERT and TEM models (i.e., Figures 8 and 11) and the other information are presented in Figure 12.

Low P-wave velocities of  $<1800$  m/s require the presence of unconsolidated sediments from the surface to  $145 \pm 10$  and  $115 \pm 10$  m depths beneath HR2 and Jao, respectively (Figure 12; Reiser et al., 2014). High resistivities of  $300\text{--}400 \Omega\text{m}$  and ubiquitous near-surface sand indicate that dry and freshwater-saturated sand occupies the upper  $\sim 29$  m of ground at HR2. During the ground-based field campaign at this site, the sand at the surface was dry (hence the thin surface layer with P-wave velocities of  $<1000$  m/s), but partially water-saturated sediments were observed at shallow depths in nearby minor topographic depressions and in seismic-source drillholes. Coincident low P-wave velocities and low  $2\text{--}3\text{-}\Omega\text{m}$  resistivities below HR2 are best interpreted as saline-water-saturated sand and clay. Freshwater overlying saline water is observed in intermediate-depth water wells at various locations throughout the delta (T. Preston, personal communication, 2011) and in boreholes near its southeastern margin. These same boreholes and the borehole on Thata Island also penetrate multiple clay layers, some as thick as 40 m (MMEWR, 2004; Milzow et al., 2009). The nature of the transition zone in Figure 8a is not established. It could be caused by gradual increases in salinity and/or clay content with depth.

The interface between unconsolidated sediments and basement at  $145 \pm 10$ -m depth (Figure 12) is well defined in the HR2 seismic refraction–reflection models by a distinct change in seismic facies, a sharp increase in P-wave velocity from  $\sim 1800$  to  $>4500$  m/s, and a strong continuous reflection (Reiser et al., 2014). To within experimental error, the discrete increase in resistivity from  $2$  to  $3 \Omega\text{m}$  to  $>15 \Omega\text{m}$  (likely  $>100 \Omega\text{m}$ ) in Figure 12a occurs at the sediment–basement interface. It is noteworthy that an equivalent resistivity increase in the regional HTEM model coincides with the sediment–basement interface intersected in a water well less than 20 km northwest of HR2 (Figure 1 in Podgorski et al., 2013b).

Lack of a thick resistive surface layer and high resistivities on both sides of the sediment–basement interface defined by the seismic refraction–reflection models distinguishes the conditions at Jao from those at HR2. Thin surface units with very low P-wave velocities of  $<1000$  m/s and high  $100\text{-}\Omega\text{m}$  resistivities (Figures 10, 11 and 12b) at Jao are consistent with the dry sandy sediments observed at the surface. Immediately beneath the dry surficial sediments, coincident low P-wave velocities of  $<1800$  m/s and low  $1\text{--}4\text{-}\Omega\text{m}$  resistivities together with occurrences of clay in some seismic-source boreholes suggest that the ground mostly comprises saline-water-saturated sand, clayey sand, and clay to  $\sim 30$ -m depth. The very shallow groundwater table at this site is a natural consequence of the flat

landscape between the recording line and nearby open water (Figure 2b). Because the substantial resistivity increase from  $1\text{--}4 \Omega\text{m}$  to  $>25 \Omega\text{m}$  (likely  $>200 \Omega\text{m}$ ) in Figure 12b does not correlate with any significant P-wave velocity changes and such an increase is not easy to explain in terms of a lithological variations alone, we interpret it in terms of a major decrease in groundwater salinity. If this explanation is correct, then one or more of the clay layers must be acting as an impermeable barrier to flow between saline-water-saturated sediments above and freshwater-saturated sediments below. The nature of the transition zone between the conductive and resistive layers in Figure 12b is not established.

Like the situation at HR2, the sediment–basement interface at Jao is well delineated by abrupt seismic facies and P-wave velocity changes and a high amplitude reflection (Reiser et al., 2014). Even if there is a resistivity increase across the contact between the interpreted freshwater sediments and basement rocks, it is unlikely that our ERT and TEM data would be substantially affected by it.

### Regional hydrogeologic and geologic models

Given the generally good correlation of the ground-based ERT/TEM and seismic refraction–reflection models with the HTEM models, the resistivity depth slices in Figure 3 can be used to extrapolate the detailed information on the depth distribution of resistivities (this study) and P-wave velocities (Reiser et al., 2014) determined at HR2 and Jao. The moderately to highly resistive heterogeneous upper layer in Figure 3b and 3d, which thickens in a northwest–southeast direction, is explained by open water (in the top few meters in many regions) and omnipresent dry to freshwater-saturated sand and clayey sand. We interpret the underlying relatively homogeneous conductive layer as intercalated deposits of saline-water-saturated sand and clay. These resistive and conductive layers extend throughout most regions of the delta, although our

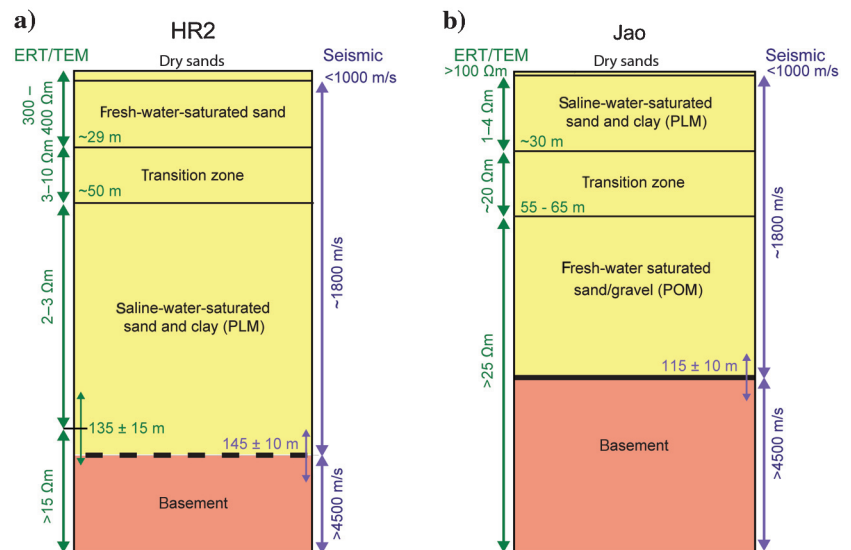


Figure 12. ERT/TEM inversion models at (a) HR2 and (b) Jao shown with the respective simplified high-resolution seismic refraction–reflection models of Reiser et al. (2014; seismic line locations are shown in Figure 2) and their geologic interpretation. Depths to layer interfaces from ERT/TEM and seismic models are shown by green and purple lines, respectively. Interpreted unconsolidated sediments and basement are yellow and orange, respectively. PLM–Paleo Lake Makgadikgadi deposits; POM–Paleo Okavango Megafan sediments (only seen below the Jao site).

investigation at Jao has demonstrated that the resistive layer is locally absent or very thin (<4 m), such that the conductive layer approaches the surface. The conductive layer in the western part of the delta appears to be in direct contact with underlying resistive basement rocks. By comparison, the conductive layer in the northern part of the delta seems to overlie a resistive sedimentary unit, interpreted to comprise freshwater-saturated sand (and possibly gravel). This lower resistive sedimentary unit likely sits directly on resistive basement rocks.

Podgorski et al. (2013b) explain the top resistive layer of dry to freshwater-saturated sand and clayey sand as sediments deposited in the alluvial megafan environment of the present Okavango Delta. They suggest that the underlying conductive layer mostly represents lacustrine clay deposited in a huge lake that would have been a northwesterly extension of Paleo Lake Makgadikgadi (PLM in Figure 12). Numerous earlier studies (Du Toit, 1927; Grove, 1969; Grey and Cooke, 1977; Cooke, 1980; Thomas and Shaw, 1991; Moore and Larkin, 2001; Huntsman-Mapila et al., 2006; Burrough et al., 2009; Moore et al., 2012) have demonstrated that Paleo Lake Makgadikgadi once covered a 66,000 km<sup>2</sup> area southeast and north of the delta. If the suggestion of Podgorski et al. (2013b) is correct, Paleo Lake Makgadikgadi would have covered an even greater area of 90,000 km<sup>2</sup>, larger than the planet's most extensive freshwater body today, Lake Superior (81,000 km<sup>2</sup>). Finally, Podgorski et al. (2013b) speculate that the arcuate-shaped nature of the electrically resistive freshwater-saturated sediments underlying the conductive layer in the northern part of the delta is a consequence of the sediments having been deposited in a Paleo Okavango Megafan (POM in Figure 12).

## CONCLUSIONS

Local resistivity models provided by independent and joint inversions of ground-based ERT and TEM data acquired at two well-separated sites are generally consistent with regional resistivity models derived from HTEM data collected across the entire Okavango Delta. These models are characterized by a general three-layer structure comprising a moderately to highly resistive heterogeneous shallow layer, a conductive relatively homogeneous intermediate-depth layer, and a resistive deep layer. Interpretation of these layers is constrained by surface geologic observations, the results of seismic refraction-reflection investigations, and diverse borehole information. For the northern part of the delta, our interpretation includes four successively deeper geologic units: (1) freshwater-saturated megafan and fluvial sediments of the current Okavango Delta (shallow resistive layer), (2) extensive saline-water-saturated sand and lacustrine clay of Paleo Lake Makgadikgadi (intermediate-depth conductive layer), (3) freshwater-saturated sand and gravel deposited in the proposed Paleo Okavango Megafan (upper part of the deep resistive layer), and (4) basement rocks (lower part of the deep resistive layer). The arcuate shape of the upper part of the deep resistive layer and its location above the seismically defined sediment-basement boundary are the principal arguments for its interpretation as the Paleo Okavango Megafan. In other regions of the delta, there is no obvious lower layer of freshwater-saturated sand and gravel, such that the layer of saline-water-saturated sand and lacustrine clay probably lies directly on basement rocks.

Future work should involve attempts to constrain inversions of the HTEM data using the ground-based TEM and ERT data as well as information on basement depths provided by the seismically de-

rived models. Finally, boreholes that penetrate the entire sedimentary column need to be considered. Although obtaining permission to drill and log relatively deep holes within the environmentally and politically sensitive Okavango Delta is likely to be a major challenge, information supplied by such holes would allow our proposed stratigraphic model and its consequences for the evolution of the Okavango Delta to be tested.

## ACKNOWLEDGMENTS

This work was financed by grants from the Swiss National Science Foundation and ETH Zürich. We thank our colleagues M. Bonamore, F. Reiser, and C. Bärlocher of ETH Zürich for helping in the field campaign. We are very grateful to O. Balapi, Department of Water Affairs, Maun, for granting us access to the DWA campsite at Jao and helping us with transport facilities within the delta. Comments from two anonymous reviewers on an earlier draft of the manuscript resulted in several improvements to the presentation.

## REFERENCES

- Albouy, Y., P. Andrieux, G. Rakotonrasoa, M. Ritz, M. Descloitres, J.-L. Join, and E. Rasolomanana, 2001, Mapping coastal aquifers by joint inversion of DC and TEM soundings — Three case histories: *Ground Water*, **39**, 87–97, doi: [10.1111/j.1745-6584.2001.tb00354.x](https://doi.org/10.1111/j.1745-6584.2001.tb00354.x).
- Auken, E., and A. V. Christiansen, 2004, Layered and laterally constrained 2D inversion of resistivity data: *Geophysics*, **69**, 752–761, doi: [10.1190/1.1759461](https://doi.org/10.1190/1.1759461).
- Auken, E., A. V. Christiansen, B. H. Jacobsen, N. Foged, and K. I. Sørensen, 2005, Piecewise 1D laterally constrained inversion of resistivity data: *Geophysical Prospecting*, **53**, 497–506, doi: [10.1111/j.1365-2478.2005.00486.x](https://doi.org/10.1111/j.1365-2478.2005.00486.x).
- Bauer, P., R. Supper, S. Zimmermann, and W. Kinzelbach, 2006, Geoelectrical imaging of groundwater salinization in the Okavango Delta, Botswana: *Journal of Applied Geophysics*, **60**, 126–141, doi: [10.1016/j.jappgeo.2006.01.003](https://doi.org/10.1016/j.jappgeo.2006.01.003).
- Bauer-Gottwein, P., B. Gondwe, L. Christiansen, D. Herckenrath, L. Kgotlhang, and S. Zimmermann, 2010, Hydrogeophysical exploration of three-dimensional salinity anomalies with the time-domain electromagnetic method (TDEM): *Journal of Hydrology*, **380**, 318–329, doi: [10.1016/j.jhydrol.2009.11.007](https://doi.org/10.1016/j.jhydrol.2009.11.007).
- Burke, K., and Y. Gunnell, 2008, The African erosion surface: A continental scale synthesis of geomorphology, tectonics, and environmental change over the past 180 million years: *Geological Society of America Memoirs*, **201**, 1–66, doi: [10.1130/2008.1201](https://doi.org/10.1130/2008.1201).
- Burrough, S. L., D. S. G. Thomas, and R. M. Bailey, 2009, Mega-lake in the Kalahari: A Late Pleistocene record of the Palaeolake Makgadikgadi system: *Quaternary Science Reviews*, **28**, 1392–1411, doi: [10.1016/j.quascirev.2009.02.007](https://doi.org/10.1016/j.quascirev.2009.02.007).
- Christiansen, A. V., E. Auken, N. Foged, and K. I. Sørensen, 2007, Mutually and laterally constrained inversion of CVES and TEM data: A case study: *Near Surface Geophysics*, **5**, 115–123, doi: [10.3997/1873-0604.2006023](https://doi.org/10.3997/1873-0604.2006023).
- Cooke, H. J., 1980, Landform evolution in the context of climatic change and neo-tectonism in the Middle Kalahari of north-central Botswana: *Transactions of the Institute of British Geographers*, **5**, 80–99, doi: [10.2307/622100](https://doi.org/10.2307/622100).
- Danielsen, J. E., T. Dahlin, R. Owen, P. Mangeya, and E. Auken, 2007, Geophysical and hydrogeologic investigation of groundwater in the Karoo stratigraphic sequence at Sawmills in northern Matabeleland, Zimbabwe: A case history: *Hydrogeology Journal*, **15**, 945–960, doi: [10.1007/s10040-007-0191-z](https://doi.org/10.1007/s10040-007-0191-z).
- Du Toit, A. L., 1927, The Kalahari and some of its problems: *South African Journal of Science*, **24**, 88–101.
- Fairhead, J. D., and R. W. Girdler, 1971, The seismicity of Africa: *Geophysical Journal of the Royal Astronomical Society*, **24**, 271–301, doi: [10.1111/j.1365-246X.1971.tb02178.x](https://doi.org/10.1111/j.1365-246X.1971.tb02178.x).
- Fitterman, D. V., and M. T. Stewart, 1986, Transient electromagnetic sounding for groundwater: *Geophysics*, **51**, 995–1005, doi: [10.1190/1.1442158](https://doi.org/10.1190/1.1442158).
- Foged, N., E. Auken, A. V. Christiansen, and K. I. Sørensen, 2013, Test-site calibration and validation of airborne and ground based TEM systems: *Geophysics*, **78**, no. 2, E95–E106, doi: [10.1190/geo2012-0244.1](https://doi.org/10.1190/geo2012-0244.1).

- Gieske, A., 1996, Vegetation driven groundwater recharge below the Okavango Delta (Botswana) as a solute sink mechanism: An indicative model: *Botswana Journal of Earth Sciences*, **3**, 33–37.
- Grey, D. R. C., and H. J. Cooke, 1977, Some problems in the Quaternary evolution of the landforms of northern Botswana: *Catena*, **4**, 123–133, doi: [10.1016/0341-8162\(77\)90014-5](https://doi.org/10.1016/0341-8162(77)90014-5).
- Grove, A. T., 1969, Landforms and climatic change in the Kalahari and Ngamiland: *Geographical Journal*, **135**, 191–212, doi: [10.2307/1796824](https://doi.org/10.2307/1796824).
- Gumbrecht, T., T. S. McCarthy, and P. Bauer, 2005, The micro-topography of the wetlands of the Okavango Delta, Botswana: *Earth Surface Processes and Landforms*, **30**, 27–39, doi: [10.1002/esp.1124](https://doi.org/10.1002/esp.1124).
- Huntsman-Mapila, P., S. Ringrose, A. W. Mackay, W. S. Downey, M. Modisi, S. H. Coetzee, J.-J. Tiercelin, A. B. Kampunzu, and C. Vanderpost, 2006, Use of the geochemical and biological sedimentary record in establishing palaeo-environments and climate change in the Lake Ngami basin, NW Botswana: *Quaternary International*, **148**, 51–64, doi: [10.1016/j.quaint.2005.11.029](https://doi.org/10.1016/j.quaint.2005.11.029).
- Hutchison, I. P. G., and D. C. Midgley, 1973, A mathematical model to aid management of outflow from the Okavango swamp, Botswana: *Journal of Hydrology*, **19**, 93–112, doi: [10.1016/0022-1694\(73\)90073-5](https://doi.org/10.1016/0022-1694(73)90073-5).
- Jupp, D. L. B., and K. Vozoff, 1975, Simple iterative methods for the inversion of geophysical data: *Geophysical Journal of the Royal Astronomical Society*, **43**, 957–972, doi: [10.1111/j.1365-246X.1975.tb06205.x](https://doi.org/10.1111/j.1365-246X.1975.tb06205.x).
- Kabii, T., 1997, Okavango - the world's largest Ramsar site, [http://www.ramsar.org/cda/en/ramsar-news-archives-1997-okavango-world/main/ramsar/1-26-45-92%5E17902\\_4000\\_0](http://www.ramsar.org/cda/en/ramsar-news-archives-1997-okavango-world/main/ramsar/1-26-45-92%5E17902_4000_0), accessed 27 May 2014.
- Loke, M. H., 1997, Rapid 2D resistivity inversion using the least-squares method RES2DINV — Program manual, Penang, Malaysia.
- Loke, M. H., and R. D. Barker, 1996, Rapid least-squares inversion of apparent resistivity pseudosections by a quasi-Newton method: *Geophysical Prospecting*, **44**, 131–152, doi: [10.1111/j.1365-2478.1996.tb00142.x](https://doi.org/10.1111/j.1365-2478.1996.tb00142.x).
- McCarthy, T. S., 2006, Groundwater in the wetlands of the Okavango Delta, Botswana, and its contribution to the structure and function of the ecosystem: *Journal of Hydrology*, **320**, 264–282, doi: [10.1016/j.jhydrol.2005.07.045](https://doi.org/10.1016/j.jhydrol.2005.07.045).
- McCarthy, T. S., 2013, The Okavango Delta and its place in the geomorphological evolution of southern Africa: *South African Journal of Geology*, **116**, 1–54, doi: [10.2113/gssajg.116.1.1](https://doi.org/10.2113/gssajg.116.1.1).
- McCarthy, T. S., and W. N. Ellery, 1994, The effect of vegetation on soil and ground water chemistry and hydrology of islands in the seasonal swamps of the Okavango Fan: Botswana: *Journal of Hydrology*, **154**, 169–193, doi: [10.1016/0022-1694\(94\)90216-X](https://doi.org/10.1016/0022-1694(94)90216-X).
- McCarthy, T. S., R. W. Green, and N. J. Franey, 1993, The influence of neotectonics on water dispersal in the northeastern regions of the Okavango swamps, Botswana: *Journal of African Earth Sciences*, **17**, 23–32, doi: [10.1016/0899-5362\(93\)90019-M](https://doi.org/10.1016/0899-5362(93)90019-M).
- Milzow, C., L. Kgotlhang, P. Bauer-Gottwein, P. Meier, and W. Kinzelbach, 2009, Regional review: The hydrology of the Okavango Delta, Botswana — Processes, data and modelling: *Hydrogeology Journal*, **17**, 1297–1328, doi: [10.1007/s10040-009-0436-0](https://doi.org/10.1007/s10040-009-0436-0).
- MMEWR (Ministry of Minerals, Energy and Water Resources), 2004, DWA Maun groundwater development project: Phase 2, resources assessment and wellfield development: Final report: Gaborone, Botswana, Botswana Department of Water Affairs.
- Modisi, M., E. Atekwana, A. Kampunzu, and T. Ngwisanyi, 2000, Rift kinematics during the incipient stages of continental extension: Evidence from the nascent Okavango rift basin, northwest Botswana: *Geology*, **28**, 939–942, doi: [10.1130/0091-7613\(2000\)28<939:RKDTIS>2.0.CO;2](https://doi.org/10.1130/0091-7613(2000)28<939:RKDTIS>2.0.CO;2).
- Moore, A. E., F. P. D. Cotterill, and F. Eckardt, 2012, The evolution and ages of Makgadikgadi palaeo-lakes: Consilient evidence from Kalahari drainage evolution South-Central Africa: *South African Journal of Geology*, **115**, 385–413, doi: [10.2113/gssajg.115.3.385](https://doi.org/10.2113/gssajg.115.3.385).
- Moore, A. E., and P. A. Larkin, 2001, Drainage evolution in south-central Africa since the breakup of Gondwana: *South African Journal of Geology*, **104**, 47–68, doi: [10.2113/104.1.47](https://doi.org/10.2113/104.1.47).
- Nyboe, N. S., F. Jørgensen, and K. I. Sørensen, 2010, Integrated inversion of TEM and seismic data facilitated by high penetration depths of a segmented receiver setup: *Near Surface Geophysics*, **8**, 467–473, doi: [10.3997/1873-0604.20100026](https://doi.org/10.3997/1873-0604.20100026).
- Oldenburg, D. W., and Y. G. Li, 1999, Estimating depth of investigation in DC resistivity and IP surveys: *Geophysics*, **64**, 403–416, doi: [10.1190/1.1444545](https://doi.org/10.1190/1.1444545).
- Podgorski, J. E., E. Auken, C. Schamper, A. V. Christiansen, T. Kalscheuer, and A. G. Green, 2013a, Processing and inversion of commercial helicopter time-domain electromagnetic data for environmental assessments and geological and hydrological mapping: *Geophysics*, **78**, no. 4, E149–E159, doi: [10.1190/geo2012-0452.1](https://doi.org/10.1190/geo2012-0452.1).
- Podgorski, J. E., A. G. Green, L. Kgotlhang, W. K. H. Kinzelbach, T. Kalscheuer, E. Auken, and T. Ngwisanyi, 2013b, Paleo megalake and paleo megafan in southern Africa: *Geology*, **41**, 1155–1158, doi: [10.1130/G34735.1](https://doi.org/10.1130/G34735.1).
- Reeves, C. V., 1972, Rifting in the Kalahari: *Nature*, **237**, 95–96, doi: [10.1038/237095a0](https://doi.org/10.1038/237095a0).
- Reiser, F., J. E. Podgorski, C. Schmelzbach, H. Horstmeyer, A. G. Green, T. Kalscheuer, H. R. Maurer, W. Kinzelbach, and G. Tshoso, 2014, Constraining helicopter electromagnetic models of the Okavango Delta with seismic-refraction and seismic-reflection data: *Geophysics*, **79**, no. 3, B123–B134, doi: [10.1190/geo2013-0278.1](https://doi.org/10.1190/geo2013-0278.1).
- Sattel, D., and L. Kgotlhang, 2004, Groundwater exploration with AEM in the Boteti area, Botswana: *Exploration Geophysics*, **35**, 147–156, doi: [10.1071/EG04147](https://doi.org/10.1071/EG04147).
- Scholz, C. H., T. A. Koczyński, and D. G. Hutchins, 1976, Evidence for incipient rifting in southern Africa: *Geophysical Journal of the Royal Astronomical Society*, **44**, 135–144, doi: [10.1111/j.1365-246X.1976.tb00278.x](https://doi.org/10.1111/j.1365-246X.1976.tb00278.x).
- Shemang, E. M., and L. N. Molwalefhe, 2009, DC resistivity and seismic refraction survey across the SE margin of Lake Ngami, NW Botswana: *Acta Geophysica*, **57**, 728–742, doi: [10.2478/s11600-009-0017-6](https://doi.org/10.2478/s11600-009-0017-6).
- Thomas, D. S. G., and P. A. Shaw, 1991, *The Kalahari environment*: Cambridge University Press, 284.
- Viezzoli, A., A. V. Christiansen, E. Auken, and K. Sørensen, 2008, Quasi-3D modeling of airborne TEM data by spatially constrained inversion: *Geophysics*, **73**, no. 3, F105–F113, doi: [10.1190/1.2895521](https://doi.org/10.1190/1.2895521).